

1 **Effect of Vertical Shear in the Zonal Wind on Equatorial Electrojet**
2 **Sidebands: An Observational Perspective Using Swarm and ICON Data**

3 **J. Sreelakshmi^{1,2}, Astrid Maute^{3,4}, Arthur D. Richmond², Geeta Vichare¹, Brian J.**
4 **Harding⁵, Patrick Alken^{3,6}**

5 ¹ Indian Institute of Geomagnetism, Navi Mumbai, India.

6 ² High Altitude Observatory, National Centre for Atmospheric Research, Boulder, CO, USA.

7 ³ Cooperative Institute for Research in Environmental Sciences, University of Colorado, Boulder, CO,
8 USA.

9 ⁴ Space Weather Prediction Center, NOAA, Boulder, CO, USA.

10 ⁵ Space Sciences Laboratory, University of California, Berkeley, CA, USA.

11 ⁶ National Center for Environmental Information, NOAA, Boulder, CO, USA.

12 Corresponding author: J. Sreelakshmi (sreelaxmij@gmail.com,

13 ORCID iD: <https://orcid.org/0000-0002-9773-9914>)

14 **Key Points:**

- 15 • First observational evidence of effect of zonal wind gradients at ~130-180 km on low-
16 latitude Equatorial Electro-Jet sideband currents.
- 17 • The altitude variation of the zonal wind gradient modulates the latitudinal variation of
18 EEJ sideband currents.
- 19 • With increasing westward wind shear, the strength of low-latitude Equatorial Electro-
20 Jet sideband current increases.

Citation:

Sreelakshmi, J., Maute, A., Richmond, A. D., Vichare, G., Harding, B. J., & Alken, P. (2024). Effect of vertical shear in the zonal wind on equatorial electrojet sidebands: An observational perspective using Swarm and ICON data. *Journal of Geophysical Research: Space Physics*, 129(10), e2024JA032678. DOI: <https://doi.org/10.1029/2024JA032678>

21 **Abstract**

22 The wind dynamo in the ionosphere leads to differential motion of ions and electrons, which
23 in turn sets up electric fields and currents. Observations show that daytime lower thermospheric
24 horizontal winds have large vertical gradients. Numerical modelling conducted approximately
25 50 years ago demonstrated that the zonal wind shears in the ~130-180 km altitude range can
26 generate off-equatorial relative minima (dips) in the daytime height-integrated eastward current
27 density, appearing as westward sidebands north and south of the equatorial electrojet (EEJ).
28 This study observationally confirms this connection for the first time by combining Ionospheric
29 CONnection explorer zonal wind profiles and Swarm latitudinal zonal currents. We
30 demonstrate observationally that the magnitude of the EEJ sideband current is proportional to
31 the strength of westward turning winds with altitude in the Pedersen conductivity dominated
32 region. Additional numerical experiments explain the importance of wind shear in different
33 altitude regions in generating the sideband current. This study contributes to the better
34 understanding of the neutral wind effect on the local current generation.

35 **Plain Language Summary**

36 The winds in the E-region ionosphere push the plasma in the presence of Earth's magnetic field,
37 causing ions and electrons to move separately, producing electric current. The low-latitude
38 ionospheric current system consists of an intense eastward current at the magnetic equator
39 (called Equatorial Electro-Jet (EEJ)) and off-equatorial reduced eastward or relative westward
40 currents (EEJ sideband currents) in both hemispheres. Modelling studies have shown that the
41 altitudinal gradient of the zonal wind is related to the strength of the EEJ sideband currents.
42 However, observational studies to validate these results have been missing to this date. This
43 study utilizes simultaneous observations from Ionospheric CONnection explorer and Swarm
44 satellites to provide insights on the connection between low-latitude winds and currents, which
45 will improve our understanding of the causes of daytime ionospheric variability.

46 **1 Introduction**

47 The equatorial electrojet (EEJ) is an enhancement of the eastward current in the dayside E-
48 region at the magnetic equator, considerably stronger than the normal large-scale daytime low-
49 latitude eastward ionospheric currents. Studies of the latitude structure of EEJ magnetic
50 perturbations, using magnetometer chains on the ground (Fambitakoye et al., 1976;
51 Fambitakoye & Mayaud, 1976a, 1976b) or satellite magnetometers at low-Earth Orbiting
52 (LEO) altitudes (Cain & Sweeney, 1973; Lühr et al., 2004; Zhou et al., 2018), have found that
53 the height-integrated eastward current density not only peaks at the magnetic equator but also
54 frequently shows local minima in strength around roughly $\pm 5^\circ$ magnetic latitude. The present
55 study investigates the source of these current reductions, which we shall refer to as EEJ
56 sideband currents.

57 Richmond (1973) developed a physical model of EEJ and demonstrated that the effect of
58 height-varying winds is largest on the currents at off-equatorial latitudes. Using this model,
59 Fambitakoye et al., (1976), abbreviated by F76 hereafter, demonstrated that the zonal wind
60 shear in the altitude regions where Pedersen conductivity dominates (~130 to 180 km) is
61 responsible for the reduction in eastward currents at low-latitudes. Reddy & Devasia, (1981)
62 also found that the vertical shears of the zonal winds can generate currents which dominate at
63 the off-equatorial latitudes. Fang et al., (2008) used TIEGCM simulations to examine the
64 influence of neutral winds in different altitude regions on the equatorial upward $E \times B$ drift and
65 the ground magnetic perturbations. Their Figure 4 shows a schematic representation of the
66 study done by Fambitakoye et al., (1976).

67 Until recently, there were no simultaneous observations of wind in the lower thermospheric
68 altitudes (~90 to 200 km) along with the height-integrated current density to observationally
69 evaluate the effect of the height variation of the zonal wind on the sideband currents as

70 suggested by F76. With the recent availability of wind observations from the MIGHTI
 71 (Michelson Interferometer for Global High-Resolution Thermospheric Imaging, Englert et al.,
 72 2017) instrument on the ICON (Ionospheric CONnection explorer, Immel et al., 2018)
 73 spacecraft, together with low-latitude current estimates from the Swarm spacecraft (Friis-
 74 Christensen et al., 2006), this hypothesis can now be tested. That is the primary purpose of this
 75 paper. After almost 50 years, there is a unique opportunity to inspect the effect of zonal wind
 76 shears on low-latitude sideband currents using the wind measurements from ICON and EEJ
 77 derived from observations by the Swarm satellites.

78 In order to understand how the winds generate currents in the ionosphere in general, a brief
 79 overview of the ionospheric electrodynamics is given. In the ionospheric E region, the
 80 thermospheric neutral winds push the ionospheric plasma in the presence of Earth's magnetic
 81 field, causing differential motion of ions and electrons, which results in wind dynamo currents.
 82 The current system is divergence-free and hence polarization electric fields and currents are
 83 established. This current system produced by the dynamo action of a non-storm-time wind
 84 system is called Solar quiet currents (Sq) flowing in the low-to-mid latitudes and along
 85 geomagnetic-field lines between the southern and northern magnetic conjugate points.

86 The ionospheric current density \mathbf{J} can be expressed using Ohm's Law as follows:

$$87 \quad \mathbf{J} = \hat{\sigma} \cdot (\mathbf{E} + \mathbf{U} \times \mathbf{B}) \quad (1)$$

88 Here, $\hat{\sigma}$ is the conductivity tensor, \mathbf{E} is the electric field, \mathbf{U} is the neutral wind, and \mathbf{B} is the
 89 ambient magnetic field. The three different conductivities are the parallel (or direct) (σ_{\parallel}), the
 90 Pedersen (σ_P), and the Hall conductivity (σ_H). Parallel conductivity is parallel to \mathbf{B} and
 91 Pedersen and Hall conductivities are perpendicular to \mathbf{B} and with currents flowing parallel and
 92 perpendicular to the electric field, respectively. We assume equipotential field lines since the
 93 parallel conductivity is several orders of magnitude greater than the perpendicular
 94 conductivities. Accordingly, ionospheric electric fields and currents are strongly organized by
 95 the geomagnetic field. During sunlit hours the Pedersen and Hall conductivities are largest at
 96 altitudes of 90-200 km, the so-called "dynamo region," where significant current can flow
 97 perpendicular to \mathbf{B} .

98 At low latitudes, the zonal component of the electric current in ionosphere mostly flows
 99 eastward during daylight hours. At the magnetic equator, the east-west component of the
 100 equatorial electric field (EEF) and the horizontal geometry of magnetic fields, along with the
 101 non-conducting atmosphere below ~ 80 km, leads to an effective zonal ionospheric
 102 conductivity, known as Cowling conductivity (Cowling effect, Chapman, 1956). This results
 103 in EEJ, which generally peaks around ~ 105 km altitude. The EEJ is accompanied by a
 104 northward magnetic perturbation at the ground and a southward perturbation at LEO spacecraft
 105 altitudes.

106 We want to note that it is a long-standing debate whether EEJ should be considered part of Sq
 107 or not (Onwumechili, 1992; Stening, 1995; Vichare et al., 2016; Yamazaki & Maute, 2017),
 108 but this distinction is not discussed in the present study. In this study we focus on the off-
 109 equatorial eastward current (i.e. $\sim 5^\circ$ off the magnetic equator) which can be reduced or even
 110 reversed (as shown by simulations, Anandarao and Raghavarao, 1987; Richmond, 1973) with
 111 day-to-day variations similar to the EEJ (Jadhav et al., 2002; Thomas et al., 2017; Zhou et al.,
 112 2018).

113 In observations, Sq and EEJ current are intermixed and therefore need to be separated if
 114 studying one of them. Lühr et al., (2004) used a second-degree spherical harmonic polynomial
 115 to separate the Sq current signal from the EEJ. The resulting magnetic signal exhibits shoulders
 116 on either side of the negative scalar magnetic field associated with the EEJ current itself. It
 117 should be noted here that the negative deflection is only true for magnetic records above the E
 118 region currents. When inverted to zonal current, these shoulders can be seen as relative
 119 westward current dips in the sheet current density (see Figure 3 of Lühr et al., 2004).

120 There are some satellite-based studies on the sideband currents seen at the flanks of the
121 magnetic equator. However, to our knowledge, there is only one ground-based study conducted
122 by Fambitakoye & Mayaud (1976a, 1976b) in this domain as it is difficult to establish and
123 maintain a sufficiently dense chain of ground magnetometers. The ground-based magnetometer
124 network has become denser over the past five decades. However, the spatial coverage provided
125 by LEO satellites is unparalleled compared to ground observatories. Satellites can cover every
126 latitude in the low-to-equatorial regions, which is crucial for estimating sideband currents. Cain
127 and Sweeney (1973) found high ‘shoulders’ at off-equatorial latitudes in the residual of total
128 magnetic field observations made by the POGO satellite, indicating the presence of sideband
129 currents. Lühr et al., (2004) deduced the horizontal distribution of height-integrated current
130 densities (I) from the CHAMP satellite residual magnetic field measurements, parameterizing
131 the meridional current profile by 81 zonally oriented line currents around the EEJ peak. They
132 found that the sideband currents are a common feature peaking on average at $\pm 5^\circ$ magnetic
133 latitude, although they also found that the sideband amplitude is sensitive to how diamagnetic
134 plasma effects are calculated. Note that Maute & Richmond (2017) and Sreelakshmi & Vichare
135 (2020) found that correcting only for magnetic perturbations due to pressure-gradient currents
136 (diamagnetic effects) without including effects of gravity-driven currents may increase rather
137 than decrease the errors. Recently, Zhou et al., (2018) comprehensively characterized the low-
138 latitude sideband currents using five years of CHAMP magnetic data. They deduced the
139 average sideband current characteristics (e.g., intensity, the latitude of peak) and its
140 dependencies on local time, season, and solar activity.

141 The reversal of EEJ either due to a reversal of EEF or due to zonal winds is commonly known
142 as Counter Electrojet or CEJ. Yamazaki et al., (2021) used simultaneous observation of EEJ
143 magnitude derived from magnetic observations by the Swarm satellite missions and horizontal
144 winds derived from ICON/MIGHTI observations to inspect the effect of local zonal winds on
145 EEJ and CEJ. Their results suggest that the vertical profile of the equatorial zonal wind can
146 modulate the equatorial electric field and may lead to the reversal of the EEJ. On average during
147 CEJ events, winds are found to be eastward and westward around ~ 110 km and ~ 140 km,
148 respectively, while the reverse is true for EEJ.

149 Thermospheric winds vary with height, latitude, longitude, and time. Solar heating produces
150 large-scale daily variations in the winds, with amplitudes that tend to increase with altitude
151 above approximately 120 km, according to modeling studies (Forbes, 2007). Upward-
152 propagating tides from the lower atmosphere strongly influence the winds below 120 km
153 (Hagan & Forbes, 2002) but tend to dissipate at higher altitudes. These tides can vary with
154 latitude more rapidly than the solar-produced winds above 130 km, but generally do not vary
155 with latitude as rapidly as the currents comprising the Equatorial Electrojet (EEJ) and its
156 sidebands. Gravity waves can have latitude scales comparable to the EEJ and its sidebands, but
157 these waves are irregular and cannot produce consistent structures in the ionospheric currents.
158 Therefore, it is unlikely that the latitude structure of the winds can be directly responsible for
159 the presence of sideband currents. However, the modeling study by F76 showed that vertical
160 shear of the zonal wind, especially in the 130-180 km altitude range, can produce sidebands
161 similar to those observed by magnetometers, without requiring latitude variations of the wind.
162 Therefore, we focus on the effects of vertical structure, which is better observed.

163 Observations clearly show that neutral winds in the thermosphere are highly variable and have
164 large vertical shears (Shepherd et al., 1993, 2012; England et al., 2022). Since the winds in the
165 lower ionosphere (100 to 200 km) are sparsely sampled, the present study could inform
166 estimates of the wind from magnetometer measurements, which are more dense than wind
167 measurements (Alken et al., 2008). In addition, Richmond's (1973) model of EEJ is used in
168 this study to investigate the importance of wind shear in different altitudinal regions using
169 ICON/MIGHTI winds and Swarm EEF.

170 Section 2 outlines the data on low-latitude currents from Swarm, zonal winds observed by
 171 ICON, and the EEJ model utilized in this study. It also covers the data selection process,
 172 methodology, and the associated errors and uncertainties. Section 3 features scatter plots with
 173 gradient of zonal winds with sideband currents, both for individual measurements and for the
 174 mean values of each variable based on data grouped according to either variable. The section
 175 also includes a discussion with two linear regression lines with one of the variable as the
 176 independent variable. The impact of the altitudinal dependence of the zonal wind gradient on
 177 sideband currents is discussed in Section 4, and conclusions are presented in Section 5.

178 **2 Data and Model**

179 **2.1 Low-latitude Currents Observed by the Swarm Satellite Mission**

180 Swarm (Friis-Christensen et al., 2006; Olsen et al., 2013) is a constellation of three polar LEO
 181 satellites (A, B, and C) launched on 22nd November 2013. All three satellites have an inclination
 182 of approximately $\sim 87^\circ$. Initially, Swarm A and C are flying side-by-side with a longitudinal
 183 difference of $\sim 1.4^\circ$ at the equator at an altitude of ~ 450 km, while Swarm B is orbiting at a
 184 higher altitude of ~ 510 km. We use the Swarm level-2 EEJ data product (Alken et al., 2013b),
 185 which gives the EEJ variations and eastward EEJ estimates. Detailed information on the
 186 retrieval of EEJ from magnetic field measurements can be found in Alken (2020). The global
 187 Sq and unmodeled magnetospheric field are assumed to be represented by a magnetic scalar
 188 potential defined in a spherical coordinate system, which is fitted orbit-by-orbit to data between
 189 $\pm(12^\circ-45^\circ)$ quasi-dipole (QD) latitude and then subtracted from the residual magnetic field.
 190 Here the residual magnetic field represents the satellite magnetic field measurements with
 191 internal (core and lithospheric) and magnetospheric contributions subtracted using the
 192 CHAOS-7.15 model (Finlay et al., 2020). No corrections are made for F-region currents
 193 associated with gravitational and pressure-gradient forces on the plasma, unlike the study of
 194 Lühr et al. (2004) that corrected for diamagnetic effects associated with plasma pressure
 195 gradients. Further, the remaining magnetic field perturbations are inverted to height-integrated
 196 magnetic-eastward current densities as described in Alken, (2020).

197 **2.2 Zonal Winds Observed by ICON/MIGHTI**

198 ICON (Immel et al., 2018) is a low-latitude satellite launched on 11th October 2019 at an
 199 altitude of ~ 600 km. The satellite orbits at an inclination of 27° , with a latitudinal coverage
 200 from about 12°S to 40°N . As ICON is a low-inclination satellite, it flies through all local times
 201 during every orbit. The MIGHTI (Englert et al., 2023) instrument onboard ICON measures
 202 Doppler shifts in naturally occurring atomic oxygen airglow emissions to estimate the neutral
 203 wind velocity. We use the version 4 of Level 2.2 data product derived from the green-line
 204 emission at 557.7 nm wavelength (Harding et al., 2017, 2023). For this study, we use
 205 geographic zonal wind observations in the height range of 95–200 km. Harding et al., (2021)
 206 validated the green-line wind data against ground meteor radar data.

207 **2.3 Data Selection and Methodology**

208 We select coincident observations of Swarm and ICON/MIGHTI during geomagnetically quiet
 209 days with (a) $K_p \leq 3+$ and between January 2020 and February 2022. Figure 1a and 1b display
 210 the 10.7 cm solar radio flux (Tapping, 2013) and K_p index (Matzka et al., 2021) for the study
 211 period. Since solar flux was below 100 sfu for most days, it is not a criterion for our data
 212 selection. The geomagnetic activity is quite low for most of the time period.

213 In order to decide whether segments of orbits from the spacecraft are sufficiently close in space
 214 and time to constitute a conjunction we use the central times and locations of these segments.
 215 The other selection criteria are as follows: (b) ICON wind measurements should be within ± 30
 216 min of Swarm equatorial measurements, and (c) the longitude of ICON wind measurements
 217 should be within $\pm 10^\circ$ of the longitude of the Swarm satellite at the magnetic equatorial
 218 crossing. Manoj et al. (2006) reported that beyond 15° longitudinal separation, the correlation

219 between EEJ intensities at the two locations is statistically insignificant. (d) The wind is
 220 measured within $\pm 5^\circ$ of the magnetic equator. (e) Only high quality wind data is chosen (wind
 221 quality factor = 1). (f) Data is chosen between 9-15 local time (LT). Even though there are local
 222 time and longitudinal variations in Equatorial Electrojet due to geomagnetic main field and
 223 neutral winds (Alken et al. 2013a, Lühr et al., 2021, Yamazaki et al. 2017), the local time
 224 window is chosen wide enough to have adequate number of conjunctions. If multiple wind
 225 profiles meet all the criteria (a–f) for a given EEJ observation, we use the average of the wind
 226 profiles.

227 We select EEJ data with height-integrated current density (I_{eq}) at the magnetic equator, of
 228 $I_{eq} \geq 25$ mA/m, to avoid the influence of weak EEJ which does not have well developed
 229 sideband currents (Thomas et al., 2017). Applying all the data selection criteria, we obtained
 230 572, 520, and 549 conjunctions between ICON and Swarm A, B, and C, respectively. It should
 231 be noted that the westward sideband currents are sensitive to the details of the procedure for
 232 Sq removal. Therefore, the following provides a detailed description of the method used to
 233 derive the zonal current based on Swarm magnetic field data.

234 Figure 2a illustrates the determination of the eastward current density (EEJ) from the residual
 235 magnetic field obtained from Swarm A on 01 December 2020, at 22:47 UT (longitude=196.74°
 236 E, LT=11:54). The solid blue line represents the residual magnetic field (which is the raw
 237 measurement minus the magnetic fields from core, lithosphere, and symmetric magnetospheric
 238 fields, as described above), while the contribution from Sq and unmodeled magnetospheric
 239 ring current fields (referred to as Sq') is depicted by the blue dashed line. The latter is subtracted
 240 from the former to obtain the Residual' shown as a blue dotted line. The magnetic field
 241 contribution from Sq currents and unmodeled magnetospheric currents is estimated by fitting
 242 a model to scalar magnetic residuals, with Sq field and its induced counterparts represented by
 243 a magnetic scalar potential for sources internal to the satellite orbit, and an external scalar
 244 potential defined for magnetospheric currents.

245 The height-integrated EEJ current density derived from the Residual' (magnetic field after
 246 subtracting Sq' contributions from the residual magnetic field) is also shown in red line in the
 247 figure. The minima I_{off} of the current density within $\pm(3-9)^\circ$ of the magnetic equator represent
 248 the sideband currents (Zhou et al., 2018). We neglect any data with an absolute difference in
 249 northern and southern value of I_{off} greater than 15 mA/m.

250 Figure 2b shows the zonal wind corresponding to the current example of Figure 2a. A least-
 251 square fitted line for the zonal wind velocities between 130 and 180 km is shown to visualize
 252 the wind behavior minimizing the influence of variability and noise. In our analysis of Swarm-
 253 ICON/MIGHTI data pairs we refer to the slope of this line as “Gradient in zonal wind velocity”
 254 (ΔU_h). One feature of interest to this study is the fact that the wind tends to be increasingly
 255 westward with increasing height above 120 km. According to the modelling results of F76, a
 256 wind that is increasingly westward above 135 km will generate height-integrated eastward
 257 currents that are stronger 10° away from the magnetic equator compared to 5° away from the
 258 equator. This contributes to the creation of a sideband-like feature in the latitudinal current
 259 profile, when added to the enhanced EEJ current driven by the EEF that F76 shows to lie mostly
 260 equatorward of 5° . The results of F76 also indicate that winds below 135 km have little effect
 261 on the difference of current between 5° and 10° magnetic latitude and therefore are not expected
 262 to have much influence on the strength of sideband currents. However, it should be noted that
 263 these low-altitude winds do affect the difference of current between 10° and the equator and
 264 therefore can influence the EEJ peak current relative to the background Sq current level.

265 **2.4 Data Errors and Uncertainties**

266 Instrumental errors are relatively small, both for the Swarm magnetometer (< 0.3 nT (Friis-
 267 Christensen et al., 2006)) and for the ICON/MIGHTI wind data (< 10 ms⁻¹ (Harding et al.,

268 2017)). However, there are considerable uncertainties in estimating sideband current strengths
269 from the magnetometer data and in using the ICON/MIGHTI observations to estimate the
270 magnetic-eastward wind at the precise time and location of the paired Swarm data. These
271 uncertainties can be considered types of data errors or measurement errors when further
272 analysing the paired conjunction data and their correlation.

273 One uncertainty is that the presence and magnitude of sideband currents may be overestimated
274 by the fitting procedure. For instance, the fact that the Residual¹ is forced toward 0 nT at low
275 latitude region poleward of $\pm 12^\circ$ QD latitude (see Figure 2a) means that any negative magnetic
276 field perturbation produced there by the eastward EEJ must be offset by positive contributions
277 from sideband currents on either side of the eastward EEJ. Furthermore, magnetic perturbations
278 on the horizontal scale of the sideband currents (corresponding roughly to a horizontal
279 wavelength of $\sim 10^\circ$ or ~ 1200 km) decay with height above the main current layer at ~ 110 km
280 altitude. The decay follows an exponential distance scale of ~ 200 km, calculated as 1200
281 $\text{km}/2\pi$. Considering the Swarm satellite's orbit at an altitude of approximately 340 km above
282 the EEJ, the magnetic perturbation diminishes to approximately 1/6 compared to its intensity
283 just above the E-region currents. Consequently, it becomes evident that other factors, such as
284 unresolved or unmodeled sources contributing to the residual magnetic field, may introduce
285 signals comparable in magnitude to the sideband signal. Among the unmodeled sources are the
286 effects of F-region pressure-gradient and gravitational currents. Therefore, accurately
287 extracting the relatively weak effects of sideband currents from the Swarm magnetic data is
288 subject to considerable uncertainty. It is difficult to quantify the magnitudes of this uncertainty
289 and the potential bias in the magnitude of the sideband currents.

290 Because the times and locations of ICON/MIGHTI wind data differ somewhat from the times
291 and locations of the Swarm observations, the wind observations differ from the true winds at
292 the Swarm locations. Currently, we lack good quantitative information about the variability of
293 the winds on the temporal and spatial scales of our data-selection procedure. However the
294 difference between the observed and true winds at Swarm locations is likely a non-negligible
295 fraction of our selected wind data. Additional wind error comes from our use of the geographic
296 zonal wind to approximate the magnetic-zonal wind which is also affected by geographic
297 meridional winds when the geomagnetic declination is significant.

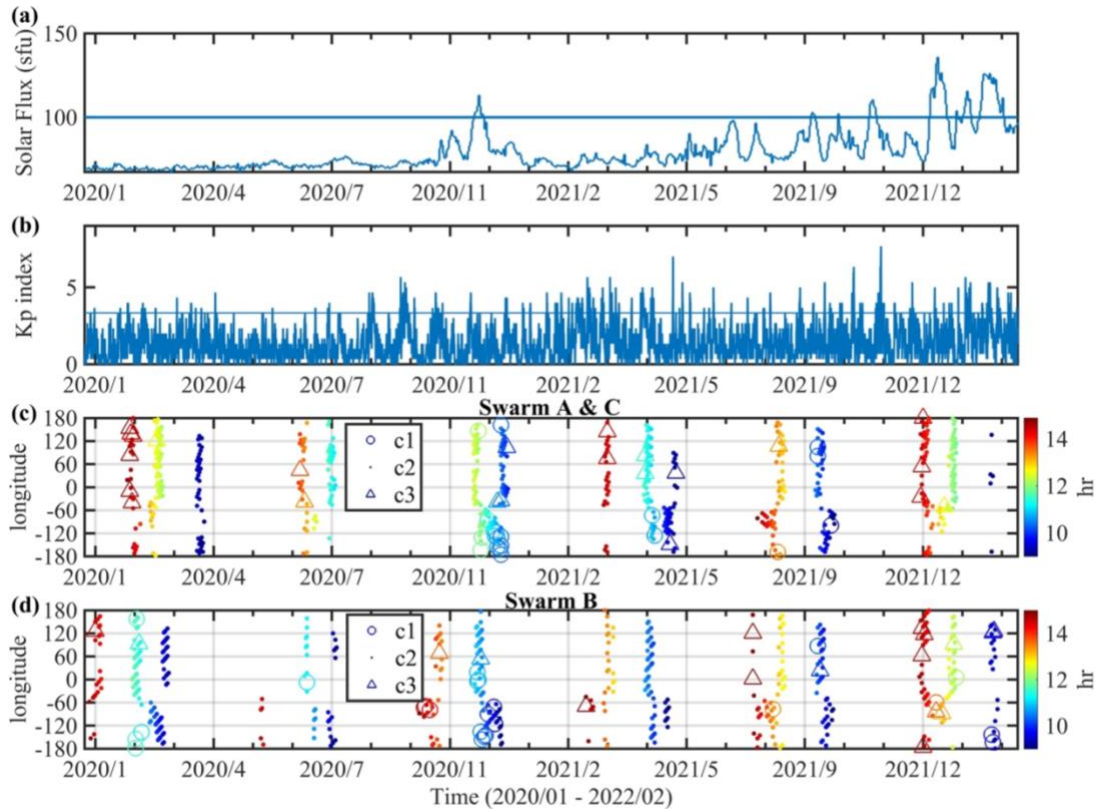
298 **2.5 EEJ model**

299 Richmond, (1973) describes a physical model of EEJ, which includes neutral winds and two-
300 stream instability. The main assumptions in this model are that 1. Longitudinal gradients of all
301 quantities are negligible, which is a reasonable approximation around ± 3 hours from noon
302 time, 2. Latitudinal gradients of the conductivities and winds are negligible, 3. Electric fields
303 do not affect the electron density, and 4. The electrojet is symmetric about the magnetic
304 equator. The model assumes a flat Earth with parabolic geomagnetic field lines and uniform
305 field strength, for which the tangent of the inclination angle is twice the tangent of the magnetic
306 latitude. Given a zonal neutral wind profile, a zonal electric field, and conductivity profiles, the
307 model computes the latitude distribution of height-integrated current, from which I_{off} can be
308 derived. See Richmond (1972, 1973) for further details on the model.

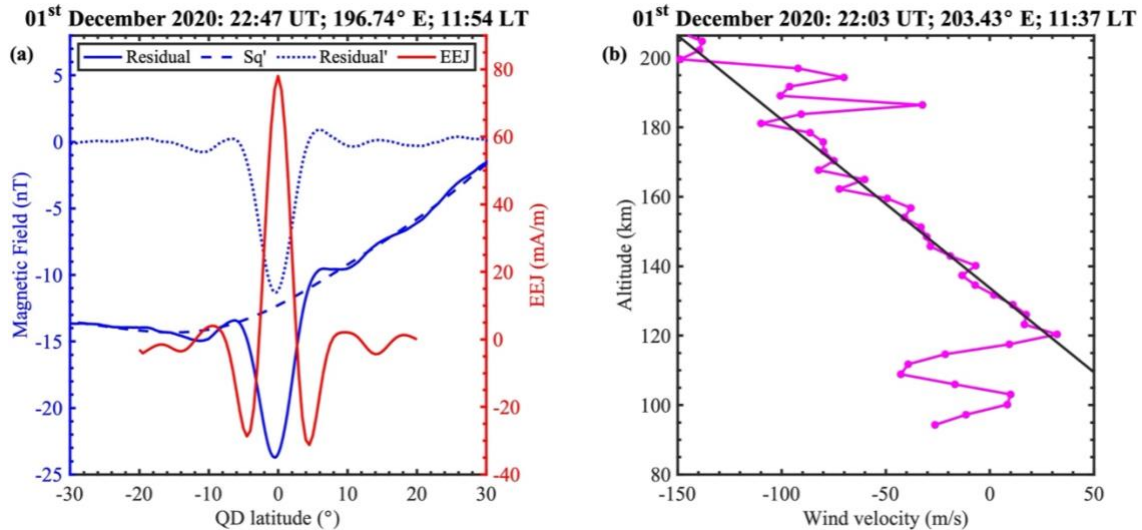
309 We use the EEJ model in the following to verify that the model can reproduce the observed
310 behaviour and to understand how the zonal wind shears at different altitudes contribute to the
311 generation of I_{off} . The wind profiles and EEF obtained from Swarm A and ICON conjunctions
312 for the three different categories are used as input into the EEJ model together with the average
313 solar flux. The currents are estimated during equinox months at 12 LT. The model will produce
314 similar results at solstice conditions since the model does not account for the latitudinal
315 gradients in the wind and conductivity. Above 200 km, we assume that the neutral wind is
316 constant with altitude. We found that the exact variation above 200 km does not influence the
317 I_{off} magnitude. This could be due to either the underestimation of F-region conductivities or

318 the non-inclusion of latitude variations of the conductivity (and wind) in the lower F region in
 319 the model.

320 To be able to compare the model results with the Swarm EEJ data, which has the Sq baseline
 321 removed, we subtract a linear baseline from the simulated height-integrated current densities,
 322 which is obtained by least-square fitting a line to values between $\pm(7^\circ$ to $10^\circ)$ dip latitude. This
 323 procedure is different from that of Swarm data since (1) in the Swarm magnetic data the Sq
 324 variation is removed while in the model, a baseline correction in current density is applied, (2)
 325 the data is fitted using spherical harmonics versus a linear fit in the model, which is appropriate
 326 for the baseline fit, and (3) the fitting procedure on data is between 12° and 45° QD latitude
 327 while the model uses values between 7° and 10° .



328
 329 Figure 1: (a) Solar activity index, 10.7 cm solar flux in sfu (solar flux units), (b) Kp index, (c)
 330 longitude of Swarm A and C in conjunction with ICON/MIGHTI, and (d) longitude of Swarm
 331 B in conjunction with ICON/MIGHTI during the period 1st January 2020 to 11th February 2022.
 332 Different symbols in (c) and (d) indicate different categories C1-C3 based on the minimum
 333 sideband current densities as described in the text, and the color indicates the local time in
 334 hours.



335
 336 Figure 2: (a) Left Y-axis shows the residual magnetic field (solid blue line), Sq': magnetic field
 337 due to Sq and unmodeled magnetospheric currents (blue dashed line) and Residual' (blue dotted
 338 line): representing the difference between residual magnetic field and Sq'. The right Y-axis
 339 illustrates the Equatorial Electrojet in mA/m (red line) (b) Altitudinal variation of zonal wind
 340 velocity in m/s, with the black line representing the least-squares line fitted to wind velocity
 341 between the altitudes 130 and 180 km.

342 3 Relating Gradients in Zonal Winds with Sideband Currents

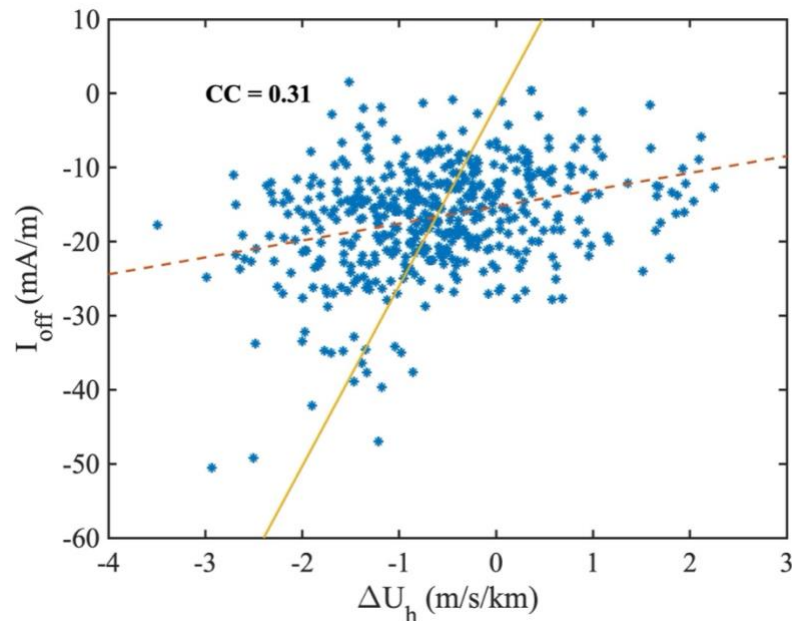
343 3.1 Scatterplot

344 Figure 3 shows the sideband current strength I_{off} and wind gradient ΔU_h for every individual
 345 pair of conjunctions between Swarm A and ICON for the selected time period. There is
 346 considerable scatter, owing to (1) potential measurement errors, especially of the wind; (2)
 347 difficulties in separating the signature of ionospheric currents from other current sources; (3)
 348 uncertainty in removing Sq currents from EEJ, (4) spatial and temporal variations of the wind
 349 and current over the windows used to select conjunctions, and (5) difficulty in determining the
 350 gradient of the highly-varying altitudinal profile of winds.

351 Nevertheless, the correlation coefficient of 0.31 is non-negligible. Because the statistical
 352 distribution of data points does not appear to represent a normal (Gaussian) distribution,
 353 standard measures of statistical significance for this correlation coefficient are not valid.
 354 However, the fact that a calculated p value using standard statistical techniques (Witte & Witte,
 355 2017) is extremely small (1.79×10^{-12}) suggests that the correlation is robust. A linear
 356 regression line fitted to these data results in a model that statistically can explain 9.61% of the
 357 sideband current strength in terms of the wind gradient. As we discuss later, when the data are
 358 binned and averaged a larger explained percentage is found for the averaged data.

359 It is not easy to find an unbiased regression line that might linearly relate I_{off} and ΔU_h , because
 360 both of the correlated variables have considerable uncertainty, and because the magnitudes of
 361 these uncertainties are not well quantified. If we were to treat one of the variables as
 362 independent and without error and then calculate a least-square regression line with the other
 363 variable, the resultant slope of the regression line would be underestimated (Riggs et al., 1978).
 364 The slope of the linear regression line when ΔU_h is treated as the independent variable (red
 365 dashed line) is ~ 2.3 As/m and that using I_{off} as the independent variable (yellow line) is ~ 24.3
 366 As/m. This substantial difference in slopes can be attributed to the impact of measurement
 367 errors in the independent variable (known as regression dilution). When ΔU_h is the independent
 368 variable, the observed slope is biased towards zero due to the increased variability introduced
 369 by measurement errors in ΔU_h . This leads to an underestimation of the true relationship

370 between ΔU_h and I_{off} . Conversely, when I_{off} is treated as the independent variable, the
 371 regression model attempts to account for the variability in I_{off} , resulting in a steeper slope. This
 372 occurs because the measurement errors in I_{off} cause the regression model to overcompensate,
 373 leading to an overestimation of the relationship between the variables. Thus, the observed
 374 disparity in the slopes highlights the critical influence of measurement errors on regression
 375 estimates, emphasizing the need for careful consideration of these errors. If the ratio of error
 376 variances of the two variables were known, it would be possible to calculate an unbiased
 377 Deming regression line (Deming, 1964), but we do not yet know the relative error variances.
 378 Instead, we explore possible quantitative relations between the winds and sideband currents by
 379 analysing the conjunction data in two different ways: organizing either in terms of I_{off} or in
 380 terms of ΔU_h .



381
 382 Figure 3: Scatter plot of gradient in ICON/MIGHTI zonal wind velocity with average of I_{off}
 383 from Swarm A in northern and southern hemisphere. The correlation coefficient CC is
 384 mentioned. Red dashed line indicates linear regression line with ΔU_h as independent variable
 385 and yellow line indicate that with I_{off} as independent variable.

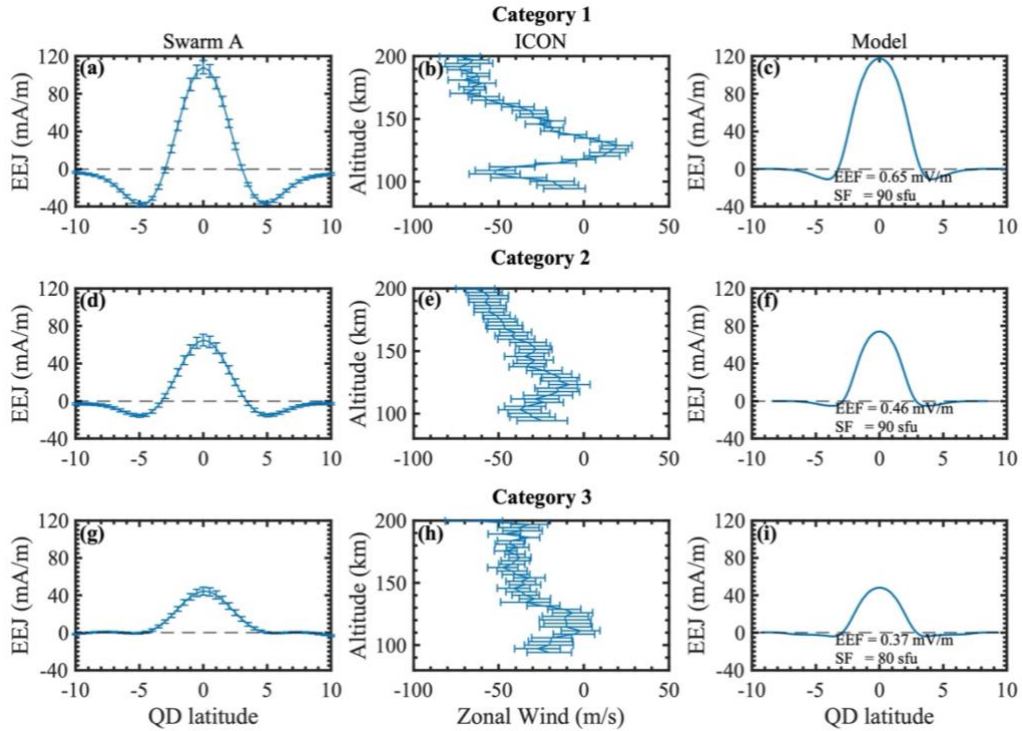
386 3.2 Grouping Data According to Sideband Current Strength

387 First, we divided the data into three categories based on the minimum height-integrated
 388 sideband current density, I_{off} defined by the following conditions for I_{off} in both hemispheres:

- 389 Category 1 (C1): $I_{off} \leq -30$ mA/m
 390 Category 2 (C2): $-30 < I_{off} \leq -5$ mA/m
 391 Category 3 (C3): $I_{off} > -5$ mA/m.

392 In C1 and C3, we have 20 and 23 conjunctions respectively, for Swarm A with ICON (Figure
 393 1c). Swarm B and C (Figure 1(c-d)) have similar numbers of conjunctions in C1 (24 & 24,
 394 respectively) and C3 (17 & 33, respectively). Meanwhile, in C2, the number of conjunctions
 395 for the Swarm satellites A, B, and C with ICON is 529, 479, and 492, respectively. The number
 396 of conjunctions in category 2 is large compared to the other two categories. Zhou et al., (2018)
 397 using CHAMP satellite data found that the sideband currents show a certain dependence on
 398 longitude with a variation of 33% between I_{off} at different longitudes. However, the Figure 1d
 399 shows that the seasonal and longitudinal distribution of the conjunctions is insufficient to be
 400 considered as an additional criterion in our analysis.

401 The first two columns of Figure 4 show the average QD latitudinal profiles of EEJ from Swarm
 402 A (left column) and the simultaneous observations of altitudinal variation of zonal winds from
 403 ICON/MIGHTI (middle). Each row is for a different category, with C1 to C3 from top to
 404 bottom. The average EEJ profile shows the largest eastward peak at the magnetic equator with
 405 two dips in both hemispheres near $\sim 5^\circ$ QD latitude. The average zonal wind is westward in the
 406 lower E region from ~ 80 to 110 km and then gets less-westward or eastward between ~ 110 to
 407 130 km. Above ~ 130 km, the wind becomes more westward with altitude.
 408 The magnitude of minimum sideband currents appears to be correlated to the gradient in zonal
 409 wind velocity estimated between 130 and 180 km. These altitudes are determined based on the
 410 fact that in general during the daytime at low latitude in the 130-180km region, the Pedersen
 411 conductivity is important.
 412 To calculate the altitude gradient of the wind for each category, the zonal wind measurement
 413 at each altitude between 130 and 180 km is selected randomly from the individual wind
 414 measurements. Then the slope is estimated using the least-square fitting on the selected values.
 415 This procedure of random selection and slope estimation is repeated 1,000,000 times and the
 416 mean is taken as the final gradient. The standard error $\left(\frac{\text{standard deviation}}{\sqrt{\text{number of samples}}} \right)$, which shows the
 417 variability of the mean of samples is estimated and shown in Figure 4(a, d, g, b, e, h) for the
 418 currents and zonal winds. As listed in Table S1, I_{off} is -37.26 mA/m for a ΔU_h of -1.64 m/s/km
 419 for category C1. For category C2, I_{off} is -15.42 mA/m, and the ΔU_h is -0.65 m/s/km. I_{off} is
 420 further reduced to -0.44 mA/m while the ΔU_h is -0.37 m/s/km for category C3. This implies
 421 that as the absolute gradient in zonal wind velocity decreases, the sideband current I_{off}
 422 decreases. This also indicates that readily available magnetic perturbation data could be used
 423 to learn about low-latitude neutral wind height variation.
 424 The third column of Figure 4 illustrates the model results. I_{eq} values are $\sim 117, 74, 48$ mA/m
 425 for the EEJ model and $\sim 108, 65, 44$ mA/m for Swarm A for C1, C2, and C3 respectively,
 426 matching well but tending to be slightly larger than the measurements. The I_{off} from Swarm
 427 are -37.26, -15.42, -0.44 mA/m and from the model are -11, -5, and -3.87 mA/m for C1, C2,
 428 C3, respectively. The I_{off} from Swarm is an average from both hemispheres while the model
 429 has a symmetric latitudinal variation. The gradient in zonal wind velocity, I_{off} and I_{eq} for the
 430 satellites and corresponding model results are summarized in Table S1.

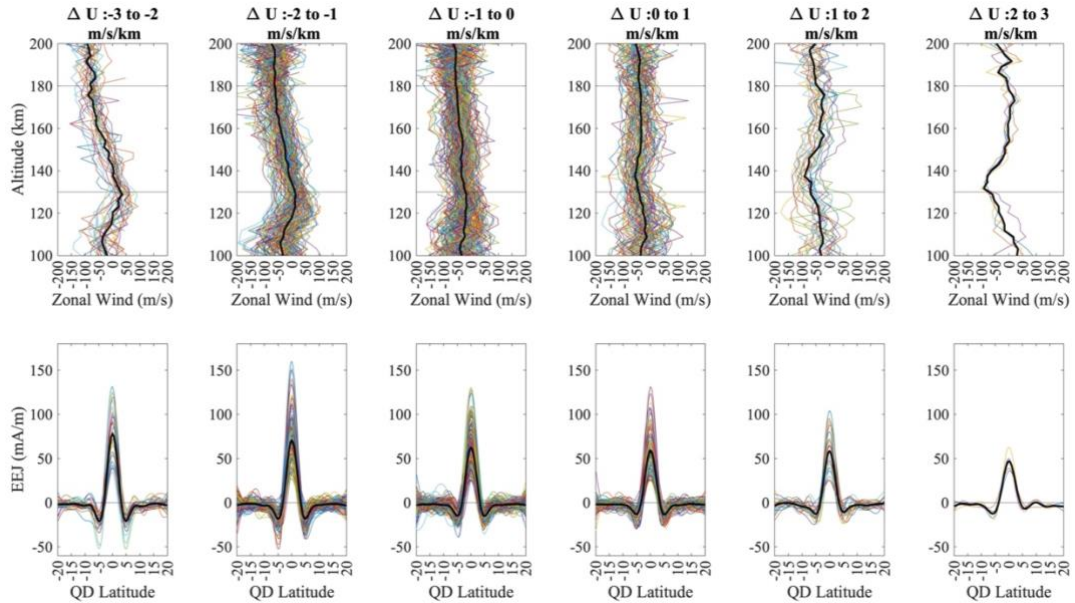


431
 432 Figure 4: The three columns are average profiles of EEJ from Swarm A, zonal wind from
 433 ICON/MIGHTI, and the corresponding EEJ from the model, respectively. This analysis is for
 434 grouping of data according to sideband current strength. Swarm EEJ and ICON zonal winds
 435 are plotted with standard errors.

436 3.3 Grouping Data According to Wind Shear

437 Next, we analysed the data by grouping it based on altitudinal gradient in zonal winds. The
 438 data are categorized based on ΔU_h in 1m/s/km bins from -3 to 3 m/s/km, resulting in six
 439 categories. Figure 5 displays the individual zonal wind measurements from ICON and EEJ
 440 from Swarm A for each category. The black line in each figure represents the corresponding
 441 mean values. For category 1, I_{off} is -20.86 mA/m for a ΔU_h of -2.32 m/s/km. In category 2,
 442 I_{off} is -18.25 mA/m with a ΔU_h -1.44 m/s/km. I_{off} is -15.04 mA/m while the ΔU_h is -0.52 m/s/km
 443 for category 3. For the categories 4, 5, and 6, I_{off} is -13.18 mA/m, -11.69 mA/m and -8.00
 444 mA/m for a ΔU_h of 0.39 m/s/km, 1.36 m/s/km and 2.12 m/s/km, respectively.

445 As the wind gradient becomes less negative or more positive, the depth of the sideband currents
 446 decreases. However, the dependence of I_{off} on ΔU_h appears much less in Figure 5 than one
 447 might expect from the relation between I_{off} and ΔU_h seen in Figure 4. Obviously, the manner
 448 in which the data are grouped has a strong effect on the derived relation between I_{off} and the
 449 wind shear. Nevertheless, the relation is positive in both cases, consistent with a real physical
 450 relation.



451
 452 Figure 5: The first row is individual zonal winds from ICON/MIGHTI and second row is EEJ
 453 from Swarm A for grouping of data according to wind shear. The black lines in each of the plot
 454 show mean Swarm EEJ and ICON zonal winds.

455 3.4 Linearity of Relation Between I_{off} and ΔU_h

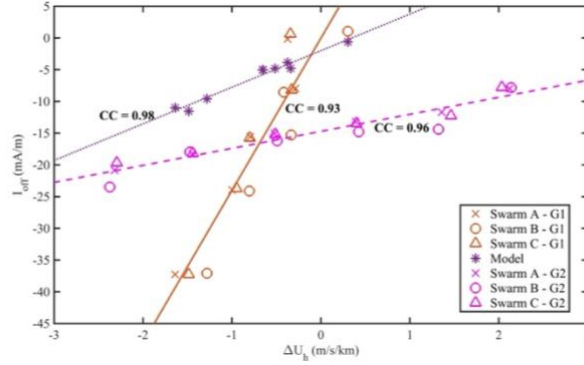
456 Given the large amount of scatter of the data from individual conjunctions seen in Figure 3, it
 457 is not obvious that the data might exhibit a linear relation between I_{off} and ΔU_h , as the physical
 458 model would predict. In this section we examine the linearity of the average relation between
 459 group-averaged conjunction data.

460 Figure 6 shows the relation between I_{off} and ΔU_h for data and model, with data from the two
 461 groupings described in sections 3.2 and 3.3. The grouping of data based on I_{off} is termed G1
 462 and that based on ΔU_h is termed G2. The model was driven by G1 group-averaged
 463 ICON/MIGHTI data. The different categories from the average conjunctions obtained from
 464 Swarm A, B, C and ICON are combined and shown for G1 in orange (solid line) and G2 in
 465 magenta (dashed line). The data for G1 was further categorized into five distinct bins with I_{off} :
 466 ≤ -30 , -30 to -20 , -20 to -13 , -13 to -5 , and > -5 mA/m. This categorization assigns 5 averages
 467 of conjunctions for each Swarm satellite A, B, and C, resulting in a total of 15 data points in
 468 Figure 6. The figure illustrates that the results for the conjunctions of Swarm B & C and ICON
 469 are consistent with the findings using Swarm A & ICON conjunctions. Similarly, G2 also
 470 shows the scatter plot of the mean ΔU_h and I_{off} for all six categories for Swarm A, B, and C
 471 conjunctions with ICON.

472 The linear correlation coefficient between I_{off} and ΔU_h is 0.93 and 0.96 for the groups, G1 and
 473 G2 respectively, meaning that on average ~ 86.5 - 92.2 % of the group-averaged I_{off} variation
 474 among the Swarm satellites and among the different cases can be explained by the group-
 475 averaged ΔU_h variation using a linear model. It should be noted here that these correlation
 476 coefficients and percent explaining variability are only valid for the averaged data in each
 477 category in the different groups, and do not necessarily apply to individual conjunctions. The
 478 large linear correlation coefficients suggest that the relation between ΔU_h and I_{off} is indeed
 479 approximately linear.

480 The physical model is compatible with the data, considering the differences between the G1
 481 and G2 analyses. The model shows a higher correlation between ΔU_h and I_{off} of 0.98 compared
 482 to the observational results. The slope of the linear regression line is ~ 5.76 As/m for the model
 483 (purple dotted line), whereas it is ~ 24 As/m and ~ 2.7 As/m for Swarm data based on the groups
 484 G1 (orange line) and G2 (magenta dashed line). If the true relation between I_{off} and the wind

485 shear is linear, then the true slope probably lies between the slopes for the G1 and G2 analyses.
 486 We suggest two possible reasons for the fact that the magnitude of I_{off} for the physical model
 487 is usually smaller than the magnitude of I_{off} for the two lines representing data groupings. (1)
 488 As noted in Section 2, the procedure for removing the effects of Sq currents from the Swarm
 489 magnetic signal may tend to overestimate the strength of the sideband currents. (2) The winds
 490 and/or conductivities may have systematic variations with magnetic latitude that are not
 491 considered in the model and could increase the magnitude of I_{off} .
 492



493
 494 Figure 6: I_{off} over the ΔU_h for Swarm-ICON observations for different categories based on I_{off}
 495 (orange) and ΔU_h (magenta). The average EEJ sideband currents from Swarm A (cross symbol),
 496 B (circle symbol), and C (triangle symbol) in conjunction with ICON winds are shown for both
 497 groupings, G1 for those based on I_{off} and G2 for ΔU_h . The line represents the linear regression
 498 line and correlation coefficient, CC is also mentioned. Purple represents the same as magenta
 499 but from the model driven by G1 group-averaged ICON/MIGHTI data.

500 4 Discussion

501 To gain further insights we examine the importance of the neutral wind gradients at different
 502 altitudes using numerical experiments and discuss the limitations of individual observational
 503 conjunctions and the model results.

504 The daytime, low-latitude zonal ionospheric current density J_ϕ due to the electric field and
 505 zonal winds in the 80 to 400 km altitude can be expressed as follows (Richmond 1973):

$$506 \quad J_\phi = \sigma_P E_\phi + \sigma_P \left[\frac{\int_{s_1}^{s_2} \sigma_H ds}{\int_{s_1}^{s_2} \sigma_P ds} \right] E_\phi + \sigma_H B U_\phi - \sigma_H B \left[\frac{\int_{s_1}^{s_2} \sigma_P U_\phi ds}{\int_{s_1}^{s_2} \sigma_P ds} \right] \quad (2)$$

507 U_ϕ is the zonal wind, and E_ϕ is the eastward EEJ. The integrals are along the magnetic field
 508 lines from foot points s_1 to s_2 at the bottom of the ionosphere. Here σ_P , σ_H , and U_ϕ are strongly
 509 height-dependent, while the magnitude of magnetic field $|B|$ varies little within the dynamo
 510 region. The first two terms on the right-hand side of equation (2) represent the current density
 511 J_E due to electric field E_ϕ , and the last two terms are the zonal wind-driven current density J_W
 512 which are the focus of this study. It is evident from the equation that the current contribution
 513 due to wind is zero if the wind is a constant along the magnetic field line.

$$514 \quad \text{Further,} \quad J_\phi = J_E + J_W \quad (3)$$

$$515 \quad \text{Or} \quad J_\phi = J_E + \sigma_H B (U_\phi - \overline{U_\phi}) \quad (4)$$

$$516 \quad \text{with} \quad \overline{U_\phi} = \frac{\int_{s_1}^{s_2} \sigma_P U_\phi ds}{\int_{s_1}^{s_2} \sigma_P ds} \quad (5)$$

517 being the field-line average zonal wind weighted by the Pedersen conductivity. By definition
 518 $\overline{U_\phi}$ is constant along a field line. We can define a perturbation wind as

$$519 \quad U'_\phi = U_\phi - \overline{U_\phi} \quad (6)$$

520 Then,

$$521 \quad J_W = \sigma_H B U'_\phi \quad (7).$$

522 Therefore, only the zonal wind perturbation with respect to the field-line average Pedersen
 523 conductivity weighted zonal wind matters in the determination of wind driven current density.
 524 In the magnetic equatorial region, the westward zonal winds at altitudes where Pedersen
 525 conductivity dominates (~130 km to 180 km) builds an upward polarization electric field to
 526 balance the vertical/meridional Pedersen current. The equipotential nature of magnetic field
 527 lines leads to the mapping of this electric field to low-latitude E region and generates eastward
 528 Hall currents (Fang et al., 2008). When these wind effects get superimposed on the effect of
 529 the eastward EEF, we get a reduction in eastward current density at low-latitudes. These
 530 reduced eastward currents become westward in nature once the background currents are
 531 removed. Further, the height-integrated current density I considered for the analysis is
 532 estimated by integrating J over all altitudes.

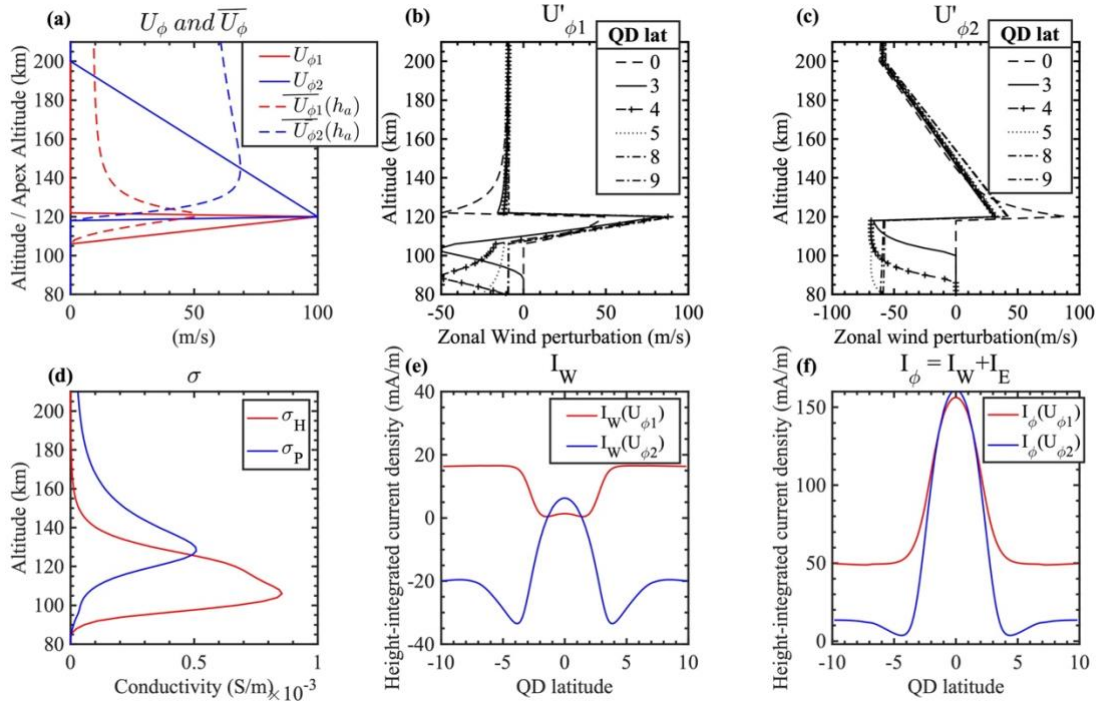
533 In Figure 7a, we take two example wind profiles (U_{ϕ_1} and U_{ϕ_2}) which are simplified from the
 534 ICON wind observations in C1 and split each into two altitude regions. Note that shifting the
 535 x-axis to the left or right is irrelevant since a constant wind in altitude does not generate any J_W
 536 as noted above. The wind profiles used are (1) U_{ϕ_1} with positive eastward wind gradient in the
 537 Hall region (~106 – 120 km), and (2), U_{ϕ_2} with negative eastward wind gradient in Pedersen
 538 region (~120 – 200 km). Both wind profiles have zero winds at altitudes other than the
 539 mentioned regions. The altitudinal variation of Hall and Pedersen conductivity is depicted in
 540 Figure 7d for reference. σ_H is dominant below 130 km while σ_P is dominant above.

541 Figure 7a also illustrates the field line averaged Pedersen conductivity weighted zonal winds
 542 (Equation 5), $\overline{U_\phi}$ over apex altitude h_a (equivalent to different field lines) using dashed lines.
 543 The perturbation winds U'_{ϕ_1} and U'_{ϕ_2} (Equation 6) are given in Fig 3b and 3c over altitude at
 544 particular QD latitudes for case 1 and 2, respectively.

545 For the wind profile U_{ϕ_1} (Figure 7a red solid curve), U'_{ϕ_1} at the equator (black dashed curve
 546 in Figure 7b) is positive below 120 km and negative in the 120 to 150 km range. This leads to
 547 a slightly positive or eastward I_W at the equator (Red curve in Figure 7e) since U'_{ϕ_1} is weighted
 548 by Hall conductivity. Even though sideband currents are generated by the neutral wind, these
 549 are too equatorward and not visible once I_E is added to I_W (Figure 7f). For increasing QD
 550 latitude, U'_{ϕ_1} is negative below 110 km and strongly positive in the 110 to 120 km altitudinal
 551 range, and almost constant negative above 120 km. The altitude integration of U'_{ϕ_1} weighted
 552 by Hall conductivity increases from QD latitude 3° to approximately 8° . Poleward of 8° , J_W
 553 becomes latitudinally independent.

554 For the wind profile U_{ϕ_2} (Figure 7a blue solid curve), U'_{ϕ_2} at QD latitude 0 (black dashed
 555 curve in Figure 7c) is zero below 120 km and positive in the 120 to 150 km range. Hence,
 556 eastward winds will produce eastward Hall currents at the equator. Increasing in QD latitude
 557 U'_{ϕ_2} are westward below 120 km and eastward in the 120 to 150 km altitudes. The dip seen in
 558 I_W (Figure 7e blue curve) at $\sim 3.8^\circ$ is generated by a minimum combining the Hall conductivity
 559 weighted westward U'_{ϕ_2} wind below 120 km with the Hall conductivity weighted eastward
 560 wind above 120 km (see the Figure 7c: 3,4, and 5° latitude). Poleward of QD latitude $\sim 7^\circ$, U'_{ϕ_2}
 561 is not changing since the apex altitude is large (above ~ 200 km), leading to a constant westward
 562 I_W (Figure 7e, blue curve). Adding I_W to I_E the dips are still visible since they occur sufficiently
 563 far from the magnetic equator (Figure 7f).

564 In summary, the dips are prevalent if the winds are becoming more westward or less eastward
 565 with increasing height in the Pedersen region, generating sideband current away from the
 566 equator, which confirms the observational results in Figures 4,5, and 6.



567
568
569
570
571
572
573
574

Figure 7: (a) Zonal winds ($U_{\phi 1}$ & $U_{\phi 2}$) with respect to altitude (h) and the average winds ($\overline{U_{\phi 1}}(h_a)$ & $\overline{U_{\phi 2}}(h_a)$) at magnetic equator with respect to apex altitude (h_a). (b & c) altitudinal profile of the wind perturbations ($U'_{\phi 1}$ & $U'_{\phi 2}$) at magnetic latitudes 0, 3, 4, 5, 8, & 9 deg. for the illustrative cases 1 and 2, respectively (d) Hall (σ_H) and Pedersen (σ_P) conductivities, (e) and (f) are height-integrated current density due to wind (I_W) alone, and both wind and electric field ($I_W + I_E$). Here red and blue color indicates the current densities for the illustrative cases 1 and 2, respectively.

575 5 Conclusions

576 The observations of Swarm and ICON conjunctions are used to examine the predictions of F76
577 and understand the effect of vertical shears of the zonal wind on low-latitude currents. The
578 following summarizes the results from this study:

- 579 a. This is the first time observational evidence has been presented connecting the zonal
580 wind shears with the low-latitude sideband currents. Although data for individual
581 conjunctions of Swarm and ICON show considerable scatter, a consistent positive
582 relation between the wind shear in the 130-180 km height range and the sideband
583 current strength is found when the data are averaged in bins grouped by either of these
584 two parameters.
- 585 b. The grouped and averaged data are correlated in a manner consistent with a linear
586 relation between the wind shear and the sideband current, as is predicted by the physical
587 model. The observations indicate that a persistent zonal wind altitude gradient in the
588 Pedersen conductivity region of ~ -1 m/s/km can generate ~ -2.68 mA/m to -24 mA/m
589 sideband current.
- 590 c. The study adds to the understanding of the effect of local winds on the low-latitude
591 current. For individual conjunctions, a linear model can explain $\sim 9.61\%$ of the sideband
592 current strength in terms of the wind gradient. When the data are grouped according to
593 wind shear and bin-averaged, $\sim 86.5 - 92.2\%$ of the sideband current variation (across
594 Swarm satellites and across categories) can be explained by the average vertical
595 gradient in the zonal wind.

- 596 d. Both the altitudinal gradient in zonal winds and the altitude at which the gradient is
 597 present control the sideband currents. Depending on the altitude at which the vertical
 598 shear in zonal winds is present, the sideband currents may or may not be present.
 599 e. The physical EEJ model aligns quantitatively with the observations. It predicts a linear
 600 relation between the sideband current strength and the wind shear, with a ratio lying
 601 between the slopes of the regression lines obtained from the averaged data that are
 602 grouped either in terms of sideband current strength or wind shear. The model sideband
 603 currents are weaker (less negative) than those estimated from the Swarm observations.
 604 This difference could be due to biases in the estimation of sideband current strength
 605 from the Swarm magnetometer data, as well as simplifications in the model.

606 **6 Open Research**

607 The Swarm Level 2 product EEF (Alken et al., 2013b), including the equatorial electrojet
 608 intensity used in this study, can be downloaded at <http://swarm-diss.eo.esa.int>. The
 609 ICON/MIGHTI Level 2.2 product Cardinal Vector Winds (Version 4) (Harding et al., 2023) is
 610 accessible from the ICON website <https://icon.ssl.berkeley.edu/Data> and SPDF
 611 (https://spdf.gsfc.nasa.gov/data_orbits.html). The geomagnetic activity index Kp (Matzka et
 612 al., 2021) was provided by the GFZ German Research Centre for Geosciences
 613 ([https://www.gfz-potsdam.de/en/section/geomagnetism/data-products-services/geomagnetic-](https://www.gfz-potsdam.de/en/section/geomagnetism/data-products-services/geomagnetic-kp-index)
 614 [kp-index](https://www.gfz-potsdam.de/en/section/geomagnetism/data-products-services/geomagnetic-kp-index)). The F10.7 index (Tapping, 2013) can be downloaded from the SPDF OMNI- Web
 615 database https://ccmc.gsfc.nasa.gov/requests/GetInput/get_indices.php. EEJ model results can
 616 be accessed without any restriction via the zenodo general repository at Sreelakshmi et al.,
 617 (2023).

618 **7 Acknowledgment**

619 We acknowledge the review provided by two anonymous reviewers, which contributed to the
 620 improvement of manuscript. JS and GV are supported by the Department of Science and
 621 Technology, Government of India. JS is also supported by NCAR/HAO Newkirk Graduate
 622 Research Fellowship. ICON is supported by NASA's Explorers Program through contracts
 623 NNG12FA45C and NNG12FA42I. AM is supported by ICON explorer NASA award
 624 80NSSC221K1990. AM and PA are supported by USPI NASA award 80NSSC21K0449,
 625 Electrojet Zeeman Imaging Explorer (EZIE). This research was supported in part NOAA
 626 cooperative agreement NA22OAR4320151. The European Space Agency (ESA) is gratefully
 627 acknowledged for providing Swarm data. This material is based upon work supported by the
 628 National Center for Atmospheric Research, which is a major facility sponsored by the National
 629 Science Foundation under Cooperative Agreement No. 1852977. We would like to
 630 acknowledge the use of computational resources (doi:10.5065/D6RX99HX) at the NCAR-
 631 Wyoming Supercomputing Center provided by the National Science Foundation and the State
 632 of Wyoming, and supported by NCAR's Computational and Information Systems Laboratory.

633 **8 References**

- 634 Alken, P., Chulliat, A., & Maus, S. (2013a). Longitudinal and seasonal structure of the
 635 ionospheric equatorial electric field. *Journal of Geophysical Research: Space*
 636 *Physics*, **118**, 1298–1305.
 637 Alken, P. (2020). Estimating Currents and Electric Fields at Low Latitudes from Satellite
 638 Magnetic Measurements. In M. W. Dunlop & H. Lühr (Eds.), *Ionospheric Multi-Spacecraft*
 639 *Analysis Tools* (pp. 233–254). Springer International Publishing.
 640 https://doi.org/10.1007/978-3-030-26732-2_11

- 641 Alken, P., Maus, S., Emmert, J., & Drob, D. P. (2008). Improved horizontal wind model
 642 HWM07 enables estimation of equatorial ionospheric electric fields from satellite magnetic
 643 measurements. *Geophysical Research Letters*, 35(11), L11105.
 644 <https://doi.org/10.1029/2008GL033580>
- 645 Alken, P., Maus, S., Vigneron, P., Sirol, O., & Hulot, G. (2013). Swarm SCARF equatorial
 646 electric field inversion chain. *Earth, Planets and Space*, 65(11), 1309–1317.
 647 <https://doi.org/10.5047/eps.2013.09.008>
- 648 Anandarao, B. G., & Raghavarao, R. (1987). Structural changes in the currents and fields of
 649 the equatorial electrojet due to zonal and meridional winds. *Journal of Geophysical*
 650 *Research*, 92(A3), 2514. <https://doi.org/10.1029/JA092iA03p02514>
- 651 Cain, J. C., & Sweeney, R. E. (1973). The POGO data. *Journal of Atmospheric and Terrestrial*
 652 *Physics*, 35(6), 1231–1247. [https://doi.org/10.1016/0021-9169\(73\)90021-4](https://doi.org/10.1016/0021-9169(73)90021-4)
- 653 Chapman, S. (1956). The electrical conductivity of the ionosphere: A review. *Il Nuovo*
 654 *Cimento*, 4(S4), 1385–1412. <https://doi.org/10.1007/BF02746310>
- 655 Deming, W. E. (1964). *Statistical adjustment of data* (Unabridged and corr. republication).
 656 Dover publ.
- 657 England, S. L., Englert, C. R., Harding, B. J., Triplett, C. C., Marr, K., Harlander, J. M.,
 658 Swenson, G. R., Maute, A., & Immel, T. J. (2022). Vertical Shears of Horizontal Winds in
 659 the Lower Thermosphere Observed by ICON. *Geophysical Research Letters*, 49(11).
 660 <https://doi.org/10.1029/2022GL098337>
- 661 Englert, C. R., Harlander, J. M., Brown, C. M., Marr, K. D., Miller, I. J., Stump, J. E., Hancock,
 662 J., Peterson, J. Q., Kumler, J., Morrow, W. H., Mooney, T. A., Ellis, S., Mende, S. B., Harris,
 663 S. E., Stevens, M. H., Makela, J. J., Harding, B. J., & Immel, T. J. (2017). Michelson
 664 Interferometer for Global High-Resolution Thermospheric Imaging (MIGHTI): Instrument
 665 Design and Calibration. *Space Science Reviews*, 212(1–2), 553–584.
 666 <https://doi.org/10.1007/s11214-017-0358-4>
- 667 Englert, C. R., Harlander, J. M., Marr, K. D., Harding, B. J., Makela, J. J., Fae, T., Brown, C.
 668 M., Ratnam, M. V., Rao, S. V. B., & Immel, T. J. (2023). Michelson Interferometer for
 669 Global High-Resolution Thermospheric Imaging (MIGHTI) On-Orbit Wind Observations:
 670 Data Analysis and Instrument Performance. *Space Science Reviews*, 219(3), 27.
 671 <https://doi.org/10.1007/s11214-023-00971-1>
- 672 Fambitakoye, O., & Mayaud, P. N. (1976a). Equatorial electrojet and regular daily variation
 673 SR—I. A determination of the equatorial electrojet parameters. *Journal of Atmospheric and*
 674 *Terrestrial Physics*, 38(1), 1–17. [https://doi.org/10.1016/0021-9169\(76\)90188-4](https://doi.org/10.1016/0021-9169(76)90188-4)
- 675 Fambitakoye, O., & Mayaud, P. N. (1976b). Equatorial electrojet and regular daily variation
 676 SR—II. the centre of the equatorial electrojet. *Journal of Atmospheric and Terrestrial*
 677 *Physics*, 38(1), 19–26. [https://doi.org/10.1016/0021-9169\(76\)90189-6](https://doi.org/10.1016/0021-9169(76)90189-6)
- 678 Fambitakoye, O., Mayaud, P. N., & Richmond, A. D. (1976). Equatorial electrojet and regular
 679 daily variation SR—III. Comparison of observations with a physical model. *Journal of*
 680 *Atmospheric and Terrestrial Physics*, 38(2), 113–121. [https://doi.org/10.1016/0021-9169\(76\)90118-5](https://doi.org/10.1016/0021-9169(76)90118-5)
- 682 Fang, T. W., Richmond, A. D., Liu, J. Y., & Maute, A. (2008). Wind dynamo effects on ground
 683 magnetic perturbations and vertical drifts. *Journal of Geophysical Research: Space Physics*,
 684 113(A11). <https://doi.org/10.1029/2008JA013513>
- 685 Finlay, C. C., Kloss, C., Olsen, N., Hammer, M. D., Tøffner-Clausen, L., Grayver, A., &
 686 Kuvshinov, A. (2020). The CHAOS-7 geomagnetic field model and observed changes in
 687 the South Atlantic Anomaly. *Earth, Planets and Space*, 72(1), 156.
 688 <https://doi.org/10.1186/s40623-020-01252-9>
- 689 Forbes, J. M. (2007). Dynamics of the Thermosphere. *Journal of the Meteorological Society*
 690 *of Japan. Ser. II*, 85B, 193–213. <https://doi.org/10.2151/jmsj.85B.193>

- 691 Friis-Christensen, E., Lühr, H., & Hulot, G. (2006). Swarm: A constellation to study the Earth's
 692 magnetic field. *Earth, Planets and Space*, 58(4), 351–358.
 693 <https://doi.org/10.1186/BF03351933>
- 694 Hagan, M. E., & Forbes, J. M. (2002). Migrating and nonmigrating diurnal tides in the middle
 695 and upper atmosphere excited by tropospheric latent heat release. *Journal of Geophysical*
 696 *Research: Atmospheres*, 107(D24). <https://doi.org/10.1029/2001JD001236>
- 697 Harding, B. J., Chau, J. L., He, M., Englert, C. R., Harlander, J. M., Marr, K. D., Makela, J. J.,
 698 Clahsen, M., Li, G., Ratnam, M. V., Bhaskar Rao, S. V., Wu, Y. J., England, S. L., & Immel,
 699 T. J. (2021). Validation of ICON-MIGHTI Thermospheric Wind Observations: 2. Green-
 700 Line Comparisons to Specular Meteor Radars. *Journal of Geophysical Research: Space*
 701 *Physics*, 126(3). <https://doi.org/10.1029/2020JA028947>
- 702 Harding, B. J., Englert, C. R., Harlander, J. M., Marr, K. D., Makela, J. M., Brown, C. M.,
 703 England, S. L., & Immel, T. J. (2023). *ICON Michelson Interferometer for Global High-*
 704 *resolution Thermospheric Imaging Wind Vectors Green* [Dataset]. NASA Space Physics
 705 Data Facility. <https://doi.org/10.48322/VTCE-7Y29>
- 706 Harding, B. J., Makela, J. J., Englert, C. R., Marr, K. D., Harlander, J. M., England, S. L., &
 707 Immel, T. J. (2017). The MIGHTI Wind Retrieval Algorithm: Description and Verification.
 708 *Space Science Reviews*, 212(1–2), 585–600. <https://doi.org/10.1007/s11214-017-0359-3>
- 709 Immel, T. J., England, S. L., Mende, S. B., Heelis, R. A., Englert, C. R., Edelstein, J., Frey, H.
 710 U., Korpela, E. J., Taylor, E. R., Craig, W. W., Harris, S. E., Bester, M., Bust, G. S.,
 711 Crowley, G., Forbes, J. M., Gérard, J.-C., Harlander, J. M., Huba, J. D., Hubert, B., ... Sirk,
 712 M. M. (2018). The Ionospheric Connection Explorer Mission: Mission Goals and Design.
 713 *Space Science Reviews*, 214(1), 13. <https://doi.org/10.1007/s11214-017-0449-2>
- 714 Jadhav, G., Rajaram, M., & Rajaram, R. (2002). A detailed study of equatorial electrojet
 715 phenomenon using Ørsted satellite observations: TECHNIQUES. *Journal of Geophysical*
 716 *Research: Space Physics*, 107(A8), SIA 12-1-SIA 12-12.
 717 <https://doi.org/10.1029/2001JA000183>
- 718 Lühr, H., Maus, S., & Rother, M. (2004). Noon-time equatorial electrojet: Its spatial features
 719 as determined by the CHAMP satellite. *Journal of Geophysical Research*, 109(A1),
 720 A01306. <https://doi.org/10.1029/2002JA009656>
- 721 Matzka, J., Stolle, C., Yamazaki, Y., Bronkalla, O., & Morschhauser, A. (2021). The
 722 Geomagnetic *Kp* Index and Derived Indices of Geomagnetic Activity. *Space Weather*,
 723 19(5). <https://doi.org/10.1029/2020SW002641>
- 724 Maute, A., & Richmond, A. D. (2017). Examining the Magnetic Signal Due To Gravity and
 725 Plasma Pressure Gradient Current With the TIE-GCM. *Journal of Geophysical Research:*
 726 *Space Physics*, 122(12). <https://doi.org/10.1002/2017JA024841>
- 727 Olsen, N., Friis-Christensen, E., Floberghagen, R., Alken, P., Beggan, C. D., Chulliat, A.,
 728 Doornbos, E., Da Encarnação, J. T., Hamilton, B., Hulot, G., Van Den IJssel, J., Kuvshinov,
 729 A., Lesur, V., Lühr, H., Macmillan, S., Maus, S., Noja, M., Olsen, P. E. H., Park, J., ...
 730 Visser, P. N. (2013). The Swarm Satellite Constellation Application and Research Facility
 731 (SCARF) and Swarm data products. *Earth, Planets and Space*, 65(11), 1189–1200.
 732 <https://doi.org/10.5047/eps.2013.07.001>
- 733 Onwumechili, C. A. (1992). Study of the Return Current of the Equatorial Electrojet. *Journal*
 734 *of Geomagnetism and Geoelectricity*, 44(1), 1–42. <https://doi.org/10.5636/jgg.44.1>
- 735 Reddy, C. A., & Devasia, C. V. (1981). Height and latitude structure of electric fields and
 736 currents due to local east-west winds in the equatorial electrojet. *Journal of Geophysical*
 737 *Research*, 86(A7), 5751. <https://doi.org/10.1029/JA086iA07p05751>
- 738 Richmond, A. D. (1972). *Numerical model of the equatorial electrojet*. Air Force Cambridge
 739 Res. Lab., Hanscom AFB, Bedford, Mass.

- 740 Richmond, A. D. (1973). Equatorial electrojet—I. Development of a model including winds
 741 and instabilities. *Journal of Atmospheric and Terrestrial Physics*, 35(6), 1083–1103.
 742 [https://doi.org/10.1016/0021-9169\(73\)90007-X](https://doi.org/10.1016/0021-9169(73)90007-X)
- 743 Riggs, D. S., Guarnieri, J. A., & Addelman, S. (1978). Fitting straight lines when both variables
 744 are subject to error. *Life Sciences*, 22(13–15), 1305–1360. [https://doi.org/10.1016/0024-](https://doi.org/10.1016/0024-3205(78)90098-X)
 745 [3205\(78\)90098-X](https://doi.org/10.1016/0024-3205(78)90098-X)
- 746 Sreelakshmi, J., Astrid Maute, Arthur D. Richmond, Geeta Vichare, Brian J. Harding, &
 747 Patrick Alken. (2023). *Effect of Vertical Shear in the Zonal Wind on Equatorial Electrojet*
 748 *Sidebands: An Observational Perspective Using Swarm and ICON Data [Dataset]*. Zenodo.
 749 <https://doi.org/10.5281/ZENODO.7639973>
- 750 Sreelakshmi, J., & Vichare, G. (2020). Gravity and Pressure-Gradient Currents Using
 751 Ionospheric Electron Density Measurements From COSMIC Satellites. *Journal of*
 752 *Geophysical Research: Space Physics*, 125(10). <https://doi.org/10.1029/2020JA028401>
- 753 Stening, R. J. (1995). What drives the equatorial electrojet? *Journal of Atmospheric and*
 754 *Terrestrial Physics*, 57(10), 1117–1128. [https://doi.org/10.1016/0021-9169\(94\)00127-A](https://doi.org/10.1016/0021-9169(94)00127-A)
- 755 Tapping, K. F. (2013). The 10.7 cm solar radio flux ($F_{10.7}$): F10.7. *Space Weather*, 11(7),
 756 394–406. <https://doi.org/10.1002/swe.20064>
- 757 Thomas, N., Vichare, G., & Sinha, A. K. (2017). Characteristics of equatorial electrojet derived
 758 from Swarm satellites. *Advances in Space Research*, 59(6), 1526–1538.
 759 <https://doi.org/10.1016/j.asr.2016.12.019>
- 760 Vichare, G., Bhaskar, A., & Ramesh, D. S. (2016). Are the equatorial electrojet and the Sq
 761 coupled systems? Transfer entropy approach. *Advances in Space Research*, 57(9), 1859–
 762 1870. <https://doi.org/10.1016/j.asr.2016.01.020>
- 763 Witte, R. S., & Witte, J. S. (2017). *Statistics*. John Wiley & Sons.
 764 [https://books.google.co.in/books?hl=en&lr=&id=KcxjDwAAQBAJ&oi=fnd&pg=PA1&ot](https://books.google.co.in/books?hl=en&lr=&id=KcxjDwAAQBAJ&oi=fnd&pg=PA1&ots=d3sXT6eO8v&sig=LrWRiyYMUGRpD0o4WUifiG-WzUc&redir_esc=y#v=onepage&q&f=false)
 765 [s=d3sXT6eO8v&sig=LrWRiyYMUGRpD0o4WUifiG-](https://books.google.co.in/books?hl=en&lr=&id=KcxjDwAAQBAJ&oi=fnd&pg=PA1&ots=d3sXT6eO8v&sig=LrWRiyYMUGRpD0o4WUifiG-WzUc&redir_esc=y#v=onepage&q&f=false)
 766 [WzUc&redir_esc=y#v=onepage&q&f=false](https://books.google.co.in/books?hl=en&lr=&id=KcxjDwAAQBAJ&oi=fnd&pg=PA1&ots=d3sXT6eO8v&sig=LrWRiyYMUGRpD0o4WUifiG-WzUc&redir_esc=y#v=onepage&q&f=false)
- 767 Yamazaki, Y., Harding, B. J., Stolle, C., & Matzka, J. (2021). Neutral Wind Profiles During
 768 Periods of Eastward and Westward Equatorial Electrojet. *Geophysical Research Letters*,
 769 48(11). <https://doi.org/10.1029/2021GL093567>
- 770 Yamazaki, Y., & Maute, A. (2017). Sq and EEJ—A Review on the Daily Variation of the
 771 Geomagnetic Field Caused by Ionospheric Dynamo Currents. *Space Science Reviews*,
 772 206(1–4), 299–405. <https://doi.org/10.1007/s11214-016-0282-z>
- 773 Zhou, Y.-L., Lüher, H., & Alken, P. (2018). The Sidebands of the Equatorial Electrojet: General
 774 Characteristic of the Westward Currents, as Deduced From CHAMP. *Journal of*
 775 *Geophysical Research: Space Physics*, 123(2), 1457–1476.
 776 <https://doi.org/10.1002/2017JA024687>
 777